Accepted Manuscript

Finite strain analysis of limestone / basaltic magma interaction and fracture: Low order mixed tetrahedron and remeshing

P. Areias, J. Carrilho Lopes, M.P. Santos, T. Rabczuk, J. Reinoso

PII: S0997-7538(18)30196-7

DOI: 10.1016/j.euromechsol.2018.09.003

Reference: EJMSOL 3651

To appear in: *European Journal of Mechanics / A Solids*

Received Date: 19 March 2018

Revised Date: 30 August 2018

Accepted Date: 7 September 2018

Please cite this article as: Areias, P., Lopes, J.C., Santos, M.P., Rabczuk, T., Reinoso, J., Finite strain analysis of limestone / basaltic magma interaction and fracture: Low order mixed tetrahedron and remeshing, *European Journal of Mechanics / A Solids* (2018), doi: https://doi.org/10.1016/j.euromechsol.2018.09.003.

Finite strain analysis of limestone / basaltic magma interaction and fracture: low order mixed tetrahedron and remeshing

P. Areias[a,b,d], J. Carrilho Lopes[a,c], M.P. Santos[a,b], T. Rabczuk[e] and J. Reinoso[•]

[a]University of Évora
Colégio Luís António Verney
Rua Romão Ramalho, 59
7002-554 Évora, Portugal

[b]Department of Physics

[c]Department of Geosciences

[d]CERIS/Instituto Superior Técnico, University of Lisbon

[e]Institute of Structural Mechanics
Bauhaus-University Weimar
Marienstraße 15
99423 Weimar, Germany

[•]Group of Elasticity and Strength of Materials
School of Engineering
University of Seville
Camino de los Descubrimientos s/n
41092, Seville, Spain

Dedicated to Professor M.P. Santos on occasion of his 65th birthday

Abstract

In this investigation, we use a recent constitutive framework and remeshing technique for tetrahedra to analyze the pressure-driven crack propagation of limestone intruded by basaltic magma. Limestone is represented by an elasto-plastic capped Drucker-Prager model with an hypoelastic term in order to account for inelastic effects from plastic signature. Kinematic hardening is considered for limestone, whereas magma is modeled by means of a compressible Bingham fluid. Classical limit surfaces of the capped model are used to initiate the crack events in the limestone. Propagation is performed by a local remeshing technique with mesh smoothing for uncracked elements. Arnold's MINI element is used to avoid locking in the quasi-incompressible case. Verification (for limestone) examples and a crack propagation example in 3D are performed. A mesh convergence study is performed, exhibiting very promising results.

KEYWORDS: dike intrusion, computational fracture, limestone basaltic magma.

1 Introduction

Modeling fracture events in rocks and geological materials is a matter of a notable importance in practical applications. Particularly, in this study, we are concerned with the interaction between basaltic magma and limestone rocks, and specifically crack propagation of limestone under the pressure effect of magma. These are called dike *intrusions* and are comprehensively described in chapter 3 of the book by Philpotts and Ague [28]. In this sense, we include here well-established features from several works on interaction. The work of Rivalta and Segall [35] where volume growth of the magma chamber due to fracture is accompanied by decrease

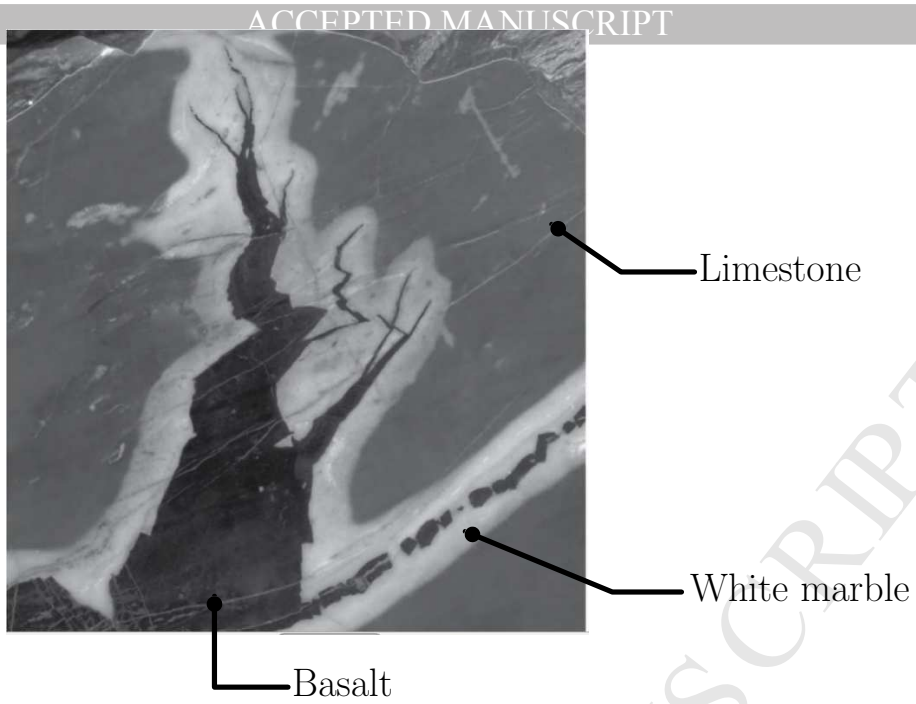

Figure 1: Gray Ordovician Trenton limestone intruded by aphanitic basalt (adapted from [28]).

in magma pressure feeding the dike. Compressibility and decompression effects are included. The concept by Clemens and Mawer [14] where (granitic) magma transport is performed by crack propagation is carried over here for the basaltic magma. As an illustration, Figure 1 is adapted from [28] and shows the result of a basaltic magma intruding in a limestone block: white marble is produced.

Although finite element solutions of magma interacting with pre-existing rock are available, as the 2D analysis by Kabele *et al.* [20], realistic crack propagation in 3D with the relevant ingredients is still not available. We have the finite element framework to perform such an analysis, see [6, 2]. Alternatives are the 3D XFEM technique [7], the strong discontinuity approach [26], phase-field technologies [24, 31, 27], dual-horizon peridynamics [32, 33] and cracking particles [30].

In this work, the focus is on intrusion of magma in basalt with a correct constitutive representation. The isothermal case is considered and we emphasize correct constitutive behavior and crack growth by a verification test.

This work is organized as follows: Section 2 presents the governing equations and a constitutive framework with modifications to our previous works, including the geometrical treatment of the back-stresses. Section 3 describes, in detail, the elasto-plastic constitutive equations and integration for the limestone model. Section 4 presents the visco-plastic constitutive model for the basalt, including the pressure term resulting from volume injection. After that, section 5 succinctly describes our remeshing algorithm, adapted for this problem. In this work, limestone cracks by element erosion, where material reaching the limit surface is replaced by magma, whose volume is increasing. Volume changes are accounted for at the constitutive level. A simple verification exercise is presented in section 6 and the adaptation of Arnold's MINI element [8] is detailed in section 7. A complete dike intrusion problem is presented in section 8. Finally, conclusions are drawn in section 9.

2 Governing equations

2.1 Equilibrium

Using conventional notation in continuum mechanics, we write the equilibrium equations as [25]:

$$\frac{\partial \sigma_{ij}}{\partial x_{_j}} + b_i = 0 \tag{1}$$

with the Cauchy tensor components being σ_{ij} $(i, j = 1, 2, 3)$. In Eq. (1) i is the direction index and j is the facet index. The components of the body force vector are b_i. Moreover, in the previous expression, x_j are the coordinates of a given point under consideration in the Lagrangian description. In addition, the following natural and essential boundary conditions hold on each part of the boundary $\Gamma = \Gamma^t \cup \Gamma^u$ where Γ^t is the natural boundary and Γ^u is the essential boundary ($\Gamma^t \cap \Gamma^u = \oslash$):

$$\overline{\boldsymbol{t}} = \boldsymbol{\sigma}\cdot\boldsymbol{v} \quad \text{on} \quad \Gamma^t \tag{2}$$
$$\overline{\boldsymbol{u}} = \boldsymbol{u} \quad \text{on} \quad \Gamma^u \tag{3}$$

where $\overline{\boldsymbol{t}}$ is the known stress vector on Γ^t where $\boldsymbol{v}$ is the outer normal and $\overline{\boldsymbol{u}}$ is the prescribed displacement field on Γ^u. As customary, conditions expressed in Eqs. (1) in the domain and (2-3) at the boundaries, are satisfied for a time parameter $t \in [0,T]$ with T being the total time of analysis and for a point with position $\boldsymbol{x} \in \Omega$ belonging to the deformed configuration at the time of analysis. Equilibrium configuration corresponds to the domain Ω. In tensor notation, equation (1) yields:

$$\boldsymbol{\nabla}\cdot\boldsymbol{\sigma}^T + \boldsymbol{b} = \boldsymbol{0} \tag{4}$$

with $\boldsymbol{\nabla} = \partial/\partial\boldsymbol{x}$ being the spatial gradient operator. After multiplication by the velocity field $\dot{\boldsymbol{u}}$, integration in the deformed configuration Ω and application of integration by parts component-wise, we obtain the following power form ($\dot{W}_{\text{int}}$ is the internal power and $\dot{W}_{\text{ext}}$ is the external power):

$$\underbrace{\int_\Omega \boldsymbol{\sigma} : \boldsymbol{l}\mathrm{d}\Omega}_{\dot{W}_{\text{int}}} = \underbrace{\int_\Omega \boldsymbol{b}\cdot\dot{\boldsymbol{u}}\mathrm{d}\Omega + \int_{\Gamma^t} \overline{\boldsymbol{t}}\cdot\dot{\boldsymbol{u}}\mathrm{d}\Gamma}_{\dot{W}_{\text{ext}}} \tag{5}$$

where $\boldsymbol{l}$, the velocity gradient reads: $\boldsymbol{l} = \frac{\partial\dot{\boldsymbol{x}}}{\partial\boldsymbol{x}} = \frac{\partial\dot{\boldsymbol{u}}}{\partial\boldsymbol{x}}$. For reasons in the corresponding algorithmic treatment, Eq (5) is written in a reference frame b (and configuration Ω_b) which is obtained by transformation (see, e.g. [2])

$$\int_{\Omega_b} \boldsymbol{S}_{ab} : \dot{\boldsymbol{e}}_{ab}\mathrm{d}\Omega_b = \dot{W}_{\text{ext}} \tag{6}$$

with the Cauchy stress being given by $\boldsymbol{\sigma} = \boldsymbol{S}_{aa} = \frac{1}{J_{ab}}\boldsymbol{F}_{ab}\boldsymbol{S}_{ab}\boldsymbol{F}_{ab}^T$. Ω_a is the current configuration and $\boldsymbol{F}_{ab}$ is the relative deformation gradient between configurations Ω_a and Ω_b. We now have to relate $\dot{\boldsymbol{e}}_{ab}$ with $\boldsymbol{l}$:

$$\underbrace{\boldsymbol{R}_{ab}^T\dot{\boldsymbol{e}}_{ab}\boldsymbol{R}_{ab}}_{\dot{\boldsymbol{e}}_{aa}} \cong \underbrace{\frac{1}{2}\left(\boldsymbol{F}_{0a}^T\dot{\boldsymbol{F}}_{a0}^T + \dot{\boldsymbol{F}}_{a0}\boldsymbol{F}_{0a}\right)}_{\boldsymbol{l}} \tag{7}$$

where Ω_0 is the initial configuration. In order to simplify the analysis herein conducted, isothermal equilibrium and crack propagation are considered (see also Balmforth *et al.* [9] who also considered the isothermal case).

2.2 Finite strain updating constitutive framework

Without loss of generality, in the present investigation, we use a specialized elasto-plastic framework which is a further development of the recent work [2], based on the regularization of the loading/unloading conditions with a specific semi-implicit integration of kinematic quantities, see also [5]. Limestone plasticity requires the use of back-stresses (a comprehensive discussion of this concept is provided by Simo and Hughes [18]). Since remeshing is performed (see [4]), the back-stress tensor should be therefore mapped between meshes. In finite strains, this implies the use of a common configuration to ensure that the correct local quantities are obtained (i.e. local frames between two successive meshes are not necessarily coincident).

In Algorithm 1, we obtain the stress tensor in frame b, $\mathbf{S}_{ab}^b$ and its sensitivity $\mathscr{C}_{ab}$ as a function of the input data $\mathbf{e}_{ab}^b$ and $\boldsymbol{R}_{0b}$. Voigt form is considered and upright bold notation is used for Voigt forms: $\mathbf{S}_{ab}^b = Voigt\left[\boldsymbol{S}_{ab}^b\right]$ (see [11]). Storage of $\mathbf{S}_{b0}^0$ (the second Piola-Kirchhoff stress in the global frame 0), $\mathbf{e}_{b0}^0$ (Green-Lagrange strain in the global frame 0) and $\mathbf{B}_{b0}^0$ (the back-stress in the global frame 0) is also required. In Algorithm 1, the transformation matrices $\mathscr{V}_s(\boldsymbol{F})$ and $\mathscr{V}_e(\boldsymbol{F})$ are given by:

$$\mathscr{V}_s(\boldsymbol{F}) = \begin{bmatrix} F_{11}^2 & F_{21}^2 & F_{31}^2 & 2F_{21}F_{11} & 2F_{31}F_{11} & 2F_{31}F_{21} \\ F_{12}^2 & F_{22}^2 & F_{32}^2 & 2F_{22}F_{12} & 2F_{32}F_{12} & 2F_{32}F_{22} \\ F_{13}^2 & F_{23}^2 & F_{33}^2 & 2F_{23}F_{13} & 2F_{33}F_{13} & 2F_{33}F_{23} \\ F_{11}F_{12} & F_{21}F_{22} & F_{31}F_{32} & F_{21}F_{12}+F_{11}F_{22} & F_{31}F_{12}+F_{11}F_{32} & F_{31}F_{22}+F_{21}F_{32} \\ F_{11}F_{13} & F_{21}F_{23} & F_{31}F_{33} & F_{21}F_{13}+F_{11}F_{23} & F_{31}F_{13}+F_{11}F_{33} & F_{31}F_{23}+F_{21}F_{33} \\ F_{12}F_{13} & F_{22}F_{23} & F_{32}F_{33} & F_{22}F_{13}+F_{12}F_{23} & F_{32}F_{13}+F_{12}F_{33} & F_{32}F_{23}+F_{22}F_{33} \end{bmatrix} \tag{8}$$

$$\mathscr{V}_e\left(\boldsymbol{F}\right) = \mathscr{V}_S^T\left(\boldsymbol{F}\right) \tag{9}$$

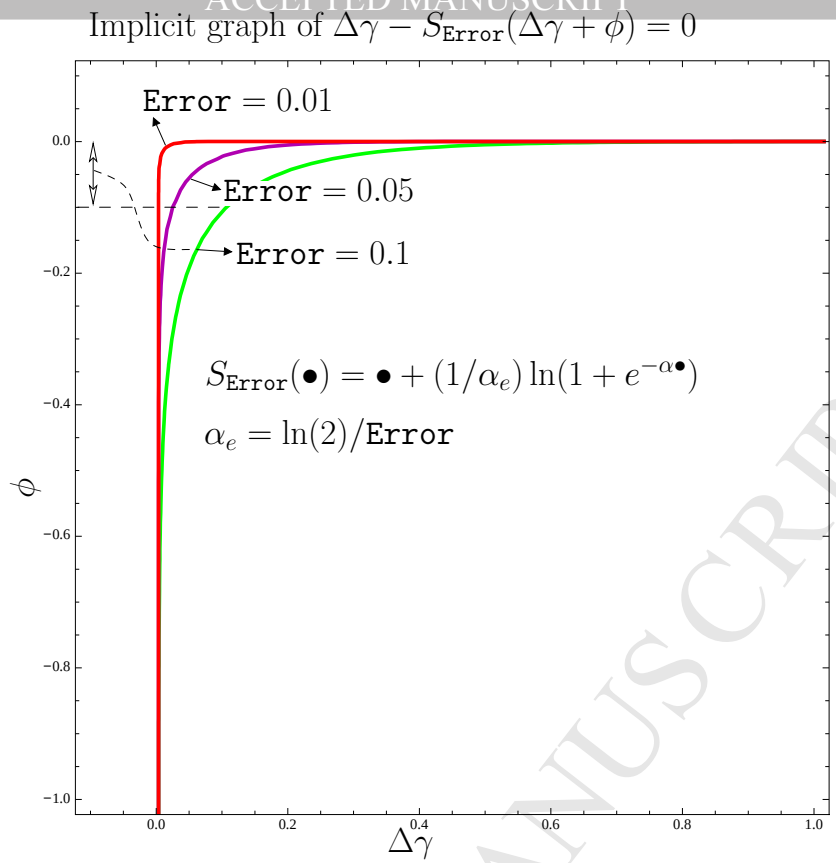

Figure 2: Replacement of $\mu^\star\Delta\gamma - \langle\mu^\star\Delta\gamma + \phi\rangle$ by $\mu^\star\Delta\gamma - S_{\texttt{Error}}(\mu^\star\Delta\gamma + \phi)$ as a function of a Error parameter ($\mu^\star = 1$ is depicted).

In this setting, in Algorithm 1, to obtain the right-stretch, use is made of a matrix square-root of $\boldsymbol{e}^b_{b0}$, $\boldsymbol{U}^b_{b0} = \sqrt{2\boldsymbol{e}^b_{b0} + \boldsymbol{I}}$ which requires a spectral decomposition. Omitting the configuration indices, to alleviate the notation, we introduce a general elasto-plastic system as:

$$\boldsymbol{\varphi}_{\texttt{Error}}(\mathbf{S}, \mathbf{e}, \mathbf{B}) = \left\{ \begin{array}{c} \mathbf{e} - \mathscr{C}^{-1}_{\text{linear}}\Delta\check{\mathbf{S}} - \mathbf{n}\Delta\gamma \\ \mu^\star\Delta\gamma - S_{\texttt{Error}}\left(\mu^\star\Delta\gamma + f\right) \\ \Delta\mathbf{B} = g(\mathbf{B}, \mathbf{S}) \end{array} \right\} \tag{10}$$

where, besides the already introduced quantities, $\mathbf{n}$ is the flow vector, $\Delta\gamma$ is the increment in the plastic multiplier, $\mu^\star > 0$ is a positive constant, f is the yield function and $S_{\texttt{Error}}$ is the Chen-Mangasarian function (see the details in [5]) represented in Figure 2.

For the kinematic hardening, $g(\mathbf{B}, \mathbf{S})$ is a function providing the increment in the back-stress. This function will be specialized later. The solution of $\boldsymbol{\varphi}(\mathbf{S}, \mathbf{e}, \mathbf{B}) = \mathbf{0}$ (10) is performed with the Newton-Raphson method at the Gauss point level.

3 Specific constitutive law for limestone

We now introduce the constitutive behavior of limestone block. Limestone is here considered a rate-independent elasto-plastic material, with a failure surface in the stress space. Two differences with the report [16] exist: temperature and rate dependence are not considered for the limestone (only in basaltic magma). Elastic behavior follows a modified Hooke law with variable bulk and shear moduli and the plastic yield function is the capped *Drucker-Prager* version. We consider a rate-independent, isotropically hardening limestone. For the elastic part of the stress, an hypoelastic law is used. We first decompose $\mathbf{S}_{ab}$ in pressure and deviatoric terms :

$$\mathbf{S}_{ab} = p_{ab}\mathbf{I} + \mathbf{S}^d_{ab} \tag{11}$$

Algorithm 1 Relative Lagrangian formulation (Voigt notation adopted) for elasto(visco) plastic materials. Frame b, reference configuration Ω_b and equilibrium configuration Ω_a.

Input data

Given $\mathbf{e}^b_{ab}$ (Voigt form) and $\boldsymbol{R}_{0b}$ Recover from storage $\mathbf{S}^0_{b0}$, $\mathbf{e}^0_{b0}$ and $\mathbf{B}^0_{b0}$

Stress/strain updating

Accumulated Green-Lagrange strain in frame b	$\mathbf{e}^b_{b0} = \mathscr{V}_e\left(\boldsymbol{R}^T_{0b}\right)\mathbf{e}^0_{b0}$
Right stretch tensor for configuration Ω_b	$\boldsymbol{U}^b_{b0} = \sqrt{2\boldsymbol{e}^b_{b0} + \boldsymbol{I}}$
Jacobian determinant	$J_{b0} = \det \boldsymbol{U}^b_{b0}$
Update total strain in frame b	$\mathbf{e}^b_{a0} = \mathbf{e}^b_{b0} + \mathscr{V}_e\left(\boldsymbol{U}^b_{b0}\right)\mathbf{e}^b_{ab}$
Stress in frame b	$\mathbf{S}^b_{bb} = \frac{1}{J_{b0}}\mathscr{V}_s\left(\boldsymbol{U}^b_{b0}\boldsymbol{R}^T_{0b}\right)\mathbf{S}^0_{b0}$
Back-stress in frame b	$\mathbf{B}^b_{bb} = \frac{1}{J_{b0}}\mathscr{V}_s\left(\boldsymbol{U}^b_{b0}\boldsymbol{R}^T_{0b}\right)\mathbf{B}^0_{b0}$

Constitutive subproblem

Determine stress and	$\mathbf{S}^b_{ab} = \mathbf{S}^b_{bb} + \Delta\check{\mathbf{S}}_a\left(\mathbf{e}^b_{ab}\right)$
back-stress	$\mathbf{B}^b_{ab} = \mathbf{B}^b_{bb} + \Delta\check{\mathbf{B}}_a\left(\mathbf{S}^b_{ab}, \mathbf{e}^b_{ab}\right)$
and sensitivity	$\mathscr{C}_{ab} = \frac{\partial\Delta\check{\mathbf{S}}_a}{\partial\mathbf{e}^b_{ab}}$

Stress updating after constitutive solution

Determine the total strain in frame 0	$\mathbf{e}^0_{a0} = \mathscr{V}_e\left(\boldsymbol{R}_{0b}\right)\mathbf{e}^b_{a0}$
Determine the second Piola-Kirchhoff stress in frame 0	$\mathbf{S}^0_{a0} = J_{b0}\mathscr{V}_s\left[\boldsymbol{R}_{0b}\left(\boldsymbol{U}^b_{b0}\right)^{-1}\right]\mathbf{S}^b_{ab}$
Back-stress stress in frame 0	$\mathbf{B}^0_{a0} = J_{b0}\mathscr{V}_s\left[\boldsymbol{R}_{0b}\left(\boldsymbol{U}^b_{b0}\right)^{-1}\right]\mathbf{B}^b_{ab}$
Store $\mathbf{S}^0_{a0}$, $\mathbf{B}^0_{a0}$ and $\mathbf{e}^0_{a0}$ Return to the element $\mathbf{S}^b_{ab}$, $\mathscr{C}_{ab}$	

where p_{ab} is the continuum mechanics pressure, $p_{ab} = {}^{\mathrm{tr}[\boldsymbol{S}_{ab}]}/_{3}$, $\mathbf{S}^d_{ab}$ is the deviatoric stress. For conciseness, we omit the configuration and frame indices. Plastic and elastic strain rates are additively decomposed:

$$\dot{\mathbf{e}} = \dot{\mathbf{e}}^p + \dot{\mathbf{e}}^e \tag{12}$$

where $\dot{\mathbf{e}}^p$ is the plastic part of the strain rate and $\dot{\mathbf{e}}^e$ is the elastic part of the strain rate. Given the bulk modulus κ and the shear modulus μ, hypoelastic relations are used to obtain the components given in Eq. 11:

$$\dot{p} = \kappa \dot{e}^e \tag{13}$$

$$\dot{\mathbf{S}}^d = 2\mu \dot{\mathbf{e}}^{de} \tag{14}$$

where $\dot{e}^e$ is the elastic volumetric strain rate and $\dot{\boldsymbol{e}}^{de}$ is the elastic deviatoric strain rate (in matrix form):

$$\dot{e}^e = \mathrm{tr}[\dot{\boldsymbol{\varepsilon}}^e] \tag{15}$$

$$\dot{\boldsymbol{e}}^{de} = \dot{\boldsymbol{e}}^e - \frac{1}{3}\boldsymbol{I}\dot{e}^e \tag{16}$$

Stress invariants are defined as usual:

$$I_1 = \mathrm{tr}\left[\boldsymbol{S}\right] = 3p \tag{17}$$

$$J_i = \frac{1}{i}\mathrm{tr}\left[\left(\boldsymbol{S}^d\right)^i\right] \tag{18}$$

We also adopt the overbar notation for I_1 and J_i: $\overline{I}_1 = -I_1$ and $\overline{J}_3 = -J_3$. Accordingly, Lode coordinates follow the definition:

$$z = \frac{I_1}{\sqrt{3}} \quad \text{axial coordinate} \tag{19}$$

$$r = \sqrt{2J_2} \quad \text{radial coordinate} \tag{20}$$

$$\sin\left(3\overline{\theta}\right) = -\frac{J_3}{2}\left(\frac{3}{J_2}\right)^{3/2} \quad \text{equation for the Lode angle} \tag{21}$$

The hypoelastic bulk modulus κ and the shear modulus μ are functions of I_1:

$$\kappa(I_1) = b_0 + b_1 \exp\left[-\frac{b_2}{|I_1|}\right] \tag{22}$$

$$\mu(I_1) = g_0\left[\frac{1 - g_1\exp\left(-g_2\sqrt{J_2}\right)}{1 - g_1}\right] \tag{23}$$

The yield function corresponds to a capped Drucker-Prager formulation, where the material parameters are estimated from experiments. The yield function can be written as [16]:

$$f = \Gamma(\overline{\theta})\sqrt{J_2} - \left[f_f\left(I_1\right) - N\right] f_c(I_1, \overline{K}, \overline{X}) \tag{24}$$

where f_f (shear term) and Γ are functions accounting for the presence of microcracks and f_c accounts for porosity and it denominated cap function. The term N in (24) identifies the initial distance to the limit function, as will become apparent. The elastic region is defined as $f < 0$. We introduce the cap function as:

$$f_c^2 = \begin{cases} 1 & -I_1 < \overline{K} \\ 1 - \left(\frac{-I_1 - \overline{K}}{\overline{X} - \overline{K}}\right)^2 & -I_1 \geq \overline{K} \end{cases} \tag{25}$$

$$= 1 - \frac{(-I_1 - \overline{K})\left(\left|-I_1 - \overline{K}\right| + (-I_1 - \overline{K})\right)}{2(\overline{X} - \overline{K})^2} \tag{26}$$

where $\overline{K}$ is the threshold of $\overline{I}_1$ from which the cap region of the yield surface is active and $\overline{X}$ is the (evolving) maximum value of $\overline{I}_1$. The flow law follows the definition:

$$\dot{\boldsymbol{e}}^p = \dot{\gamma} \underbrace{\frac{\partial f(\boldsymbol{S})}{\partial \boldsymbol{S}}}_{\boldsymbol{n}} \tag{27}$$

from which the equivalent strain is obtained.

$$\overline{\varepsilon}_v^p = \int_0^T \underbrace{\mathrm{tr}\left[\dot{\boldsymbol{e}}^p\right]}_{\dot{\overline{\varepsilon}}_v^p} \mathrm{d}t \tag{28}$$

The shear term in (24) is written as:

$$f_f = a_1 - a_3 \exp\left[-a_2 \overline{I}_1\right] + a_4 \overline{I}_1 \tag{29}$$

We use the Gudehus function for the dependence on the Lode angle:

$$\Gamma[\overline{\theta}] = \frac{1}{2}\left\{1 + \sin\left(3\overline{\theta}\right) + \frac{1}{\psi}\left[1 - \sin\left(3\overline{\theta}\right)\right]\right\}, \quad {}^7\!/_9 < \psi < {}^9\!/_7 \tag{30}$$

with ψ being an additional constitutive property. The relation between $\overline{X}$ and $\overline{\varepsilon}_v^p$ is given by inverting the expression in [16] with the crushing curve:

$$\overline{X} = -p_0 + \frac{\log\left[\frac{p_3}{p_3 - \overline{\varepsilon}_v^p}\right]}{p_1} \tag{31}$$

where p_3 is the maximum attainable volumetric strain (equivalent to initial porosity). When $\overline{\varepsilon}_v^p \geq p_3$, the model is no longer significant and a post-localization constitutive law is typically used. We note that the parameter p_2 described in [16] is not used here. In [15], the Authors used a re-worked version of (31). The relation between $\overline{K}$ and $\overline{X}$ is ruled by a shift relationship: :

$$\overline{K} = \overline{X} - R f_f \tag{32}$$

where R is the eccentricity of the cap function. In summary, Table 1 shows the relevant properties for the current Salem limestone.

Kinematic hardening is now considered. We use the back stress $\boldsymbol{B}$ and use the corrected stress

$$\boldsymbol{\xi} = \boldsymbol{S} - \boldsymbol{B} \tag{33}$$

The following law for $\boldsymbol{B}$ is used, according to [16]:

$$\dot{\boldsymbol{B}} = H G(\boldsymbol{B}) \left[\dot{\boldsymbol{e}}^p - \frac{1}{3}\boldsymbol{I}\mathrm{tr}\left(\dot{\boldsymbol{e}}^p\right)\right] \tag{34}$$

with $G(\boldsymbol{B})$ being the retarding function:

$$G(\boldsymbol{B}) = 1 - \frac{\sqrt{J_2^B}}{N} \tag{35}$$

where H is a new constitutive property. Time integration and Newton iteration on (34) for fixed $\Delta \mathrm{dev}\boldsymbol{e}^p = \Delta \boldsymbol{e}^p - \frac{1}{3}\boldsymbol{I}\mathrm{tr}\left(\Delta \boldsymbol{e}^p\right)$ results, for iteration n, as:

$$\boldsymbol{B}_{n+1} = \boldsymbol{B}_n + \left[\boldsymbol{I} - H\left(\Delta \mathrm{dev}\boldsymbol{e}^p\right) \otimes \frac{\partial G}{\partial \boldsymbol{B}}\right]^{-1} \left[-\boldsymbol{B}_{n+1} + \boldsymbol{B}_n + H G(\boldsymbol{B}_n) \Delta \mathrm{dev}\boldsymbol{e}^p\right] \tag{36}$$

The yield function including back-stress is therefore given by:

$$f = \Gamma(\overline{\theta}_{\boldsymbol{\xi}}) \sqrt{J_{2\boldsymbol{\xi}}} - \left[f_f\left(I_1\right) - N\right] f_c(I_1, \overline{K}, \overline{X}) \tag{37}$$

Table 1: Salem limestone properties

Mechanical properties obtained from [16]

Prop.	*Description*	*Value*	*Units*
b_0	Initial bulk modulus	13×10^9	Pa
b_1	$b_0 + b_1$ is the bulk modulus asymptote at high pressure	42.47×10^9	Pa
b_2	Bulk modulus curvature parameter	0.4107×10^9	Pa
g_0	Initial shear modulus	9.86×10^9	Pa
g_1	Shear modulus will have an asymptote equal to $g_0/(1-g_1)$	0	–
g_2	Shear modulus curvature parameter	0	Pa^{-1}
a_1	Parameters for the shear yield function	843.02×10^6	Pa
a_2		2.731×10^{-10}	Pa^{-1}
a_3		821.92×10^6	Pa
a_4		1×10^{-10}	–
p_0	Initial value of $-\overline{I}_1$ at collapse	-314.4×10^6	Pa
p_1	Proportional to slope of porosity vs. pressure	1.22×10^{-10}	Pa^{-1}
p_3	Initial value of porosity	0.084	–
R	Eccentricity of the cap function	6	–
ψ	Triaxial extension to compression	0.72	–
N	Initial shear yield shift	12×10^6	Pa
H	Kinematic hardening parameter	1×10^{11}	Pa
$I_1^{\max}$	Limit value of the first invariant (limit in tension)	3×10^6	Pa

In (37), $\overline{\theta}_{\boldsymbol{\xi}}$ is obtained by specializing the invariants J_2 and J_3 for the tensor $\boldsymbol{\xi}$:

$$\sin\left(3\overline{\theta}_{\boldsymbol{\xi}}\right) = -\frac{J_{3\boldsymbol{\xi}}}{2}\left(\frac{3}{J_{2\boldsymbol{\xi}}}\right)^{3/2} \tag{38}$$

We therefore have three competing limit criteria:

- Failure by crushing: $d_\varepsilon = \frac{\overline{\varepsilon}_v^p}{p_3} \geq 1$.
- Failure by shear: $d_s = \frac{\Gamma(\overline{\theta})\sqrt{J_2}}{f_f(I_1)} \geq k$ with $k < 1$ being a constitutive parameter.
- Failure by tension $d_p = \frac{I_1}{I_1^{\max}} \geq 1$.

Figure 3 shows the representation of the yield function in the $-I_1, \sqrt{J_2}$ space. Also shown are the two limiting surfaces, with failure by shear (with $\kappa = 1$) and by tension.

The effect of isotropic hardening as a function of $p_3/\overline{\varepsilon}_v^p$ is shown in Figure 4a and the effect of kinematic hardening is shown in Figure 4b. It is observable that, in terms of proximity to the failure surfaces, isotropic hardening is innocuous and kinematic hardening can result in shear failure.

Including the effect of Γ, we represent the yield function in the $\sin\left(3\overline{\theta}\right), -I_1, \sqrt{J_2}$ space. Figure 5 depicts the yield function with the effect of $\sin\left(3\overline{\theta}\right)$.

4 Constitutive law for basaltic magma

The second material under study is basaltic magma, where a non-Newtonian fluid is here considered, specifically with Bingham rheology. This behavior is known to be representative of magma in a significant range of temperatures [19, 38]. Since a strictly rigid "elastic" behavior is difficult to implement, a small elastic region is introduced. Previous works such as Walsh and Saar [40] and Piombo and Dragoni [29] follow analogous constitutive approaches. A comprehensive characterization with magma flowing in a open channel was performed

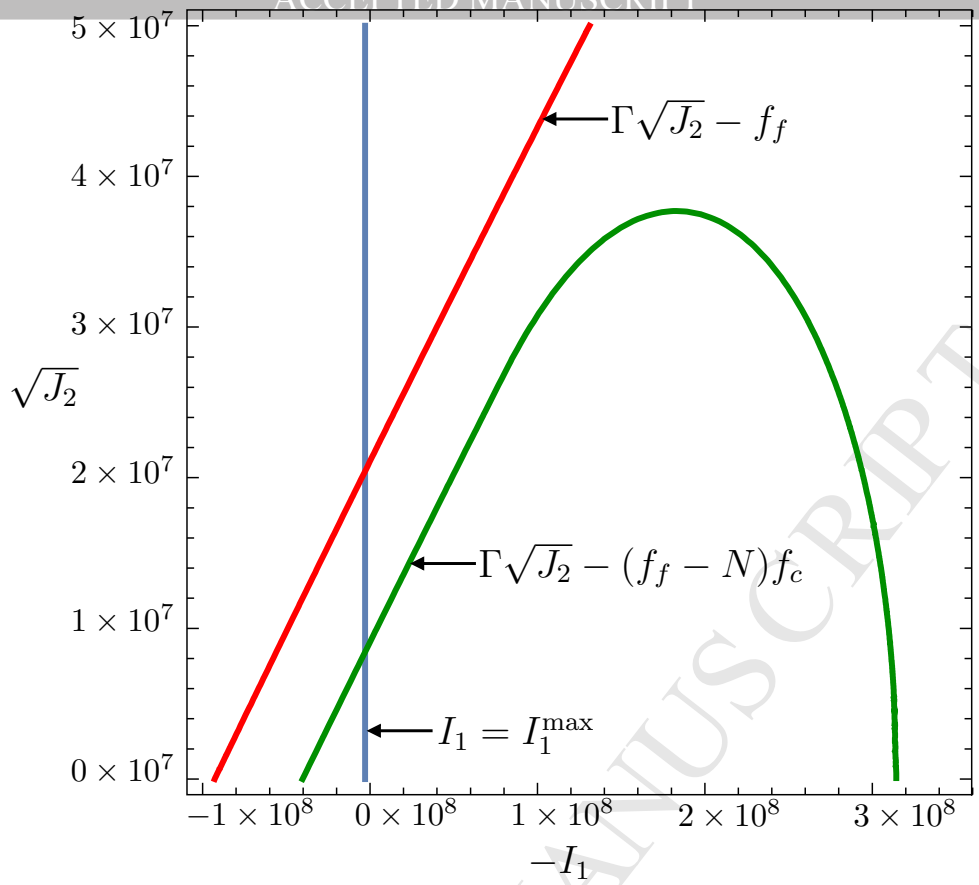

Figure 3: Limestone yield surface in $-I_1, \sqrt{J_2}$ space. We use $\sin(3\overline{\theta}) = 1$ and $N = 0$ (no kinematic hardening).

by Lev, Spiegelman, and Wysocki [22] where 3D finite elements were employed with the experimental setting image.

We therefore use a J_2 plasticity formulation with rate dependence, corresponding to the intended behavior. Recalling the previous considerations, the corresponding stress tensor of the model can be decomposed as follows:

$$\boldsymbol{S} = \overline{p}\boldsymbol{I} + \boldsymbol{S}^d \tag{39}$$

We use the dependence of the viscosity as a function of temperature measured for Grímsvötn basaltic magma [17], omitting the strain rate dependence. We are focusing on quasi-static applications and therefore only the temperature dependence is included:

$$\frac{\eta}{\text{Pa.s}} = \exp\left(P_1 + \frac{P_2}{T}\right) \tag{40}$$

where $P_1 = -38$ and $P_2 = 62 \times 10^3$ K. At this stage we use $T = 1448$ K. The yield function is now given by:

$$f = \sqrt{\frac{1}{2}\boldsymbol{S}^d : \boldsymbol{S}^d} - y - \eta\dot{\bar{\varepsilon}}_p \tag{41}$$

This yield function is a variant of the von-Mises [36] and subject to the same treatment. Specifically, the Algorithm in page 152 of Simo and Hughes [36] is adopted. Since magma is the driving force for the cracking of limestone, pressure in (39) has two sources. The decomposition into constitutive and imposed pressure makes use of the following notation:

$$\overline{p} = p_c - p_i \tag{42}$$

where p_c is the constitutive pressure, $p_c = \kappa e_e$ where e_e is the integrated elastic strain and κ is the bulk modulus. We also have $p_i = \kappa\frac{\chi V_i}{V}$ as the imposed pressure, where V is the undeformed volume and V_i is the imposed volume variation, multiplied here by the proportionality value χ.

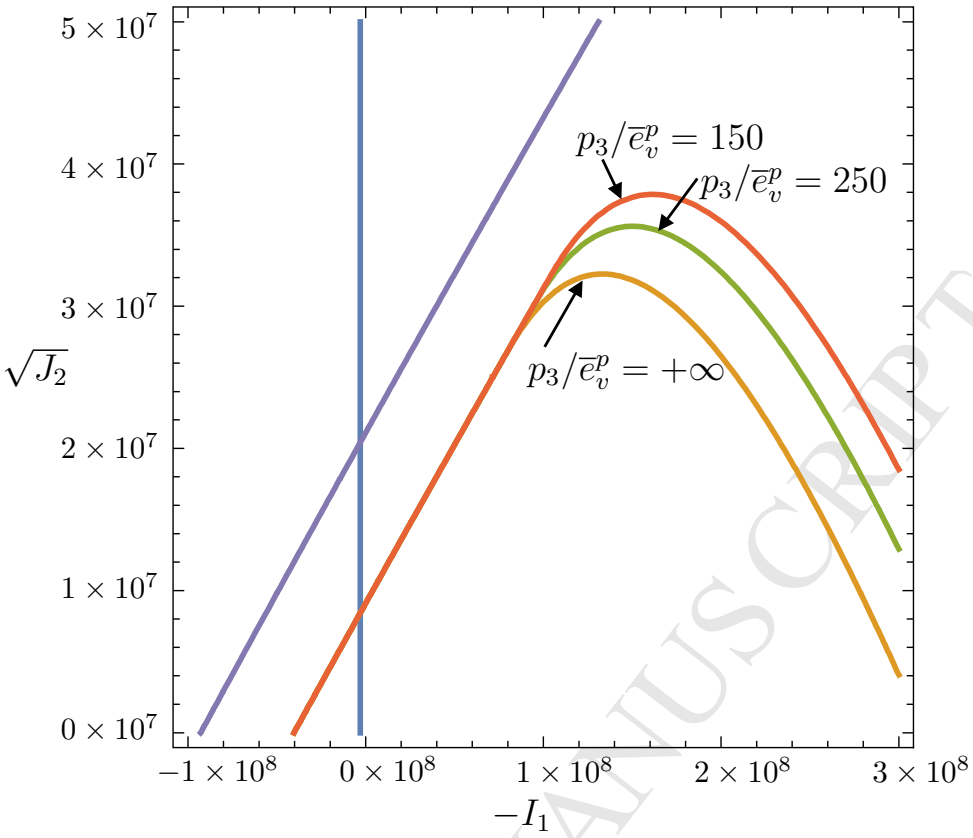

(a) Effect of isotropic hardening. $N = 12$ MPa.

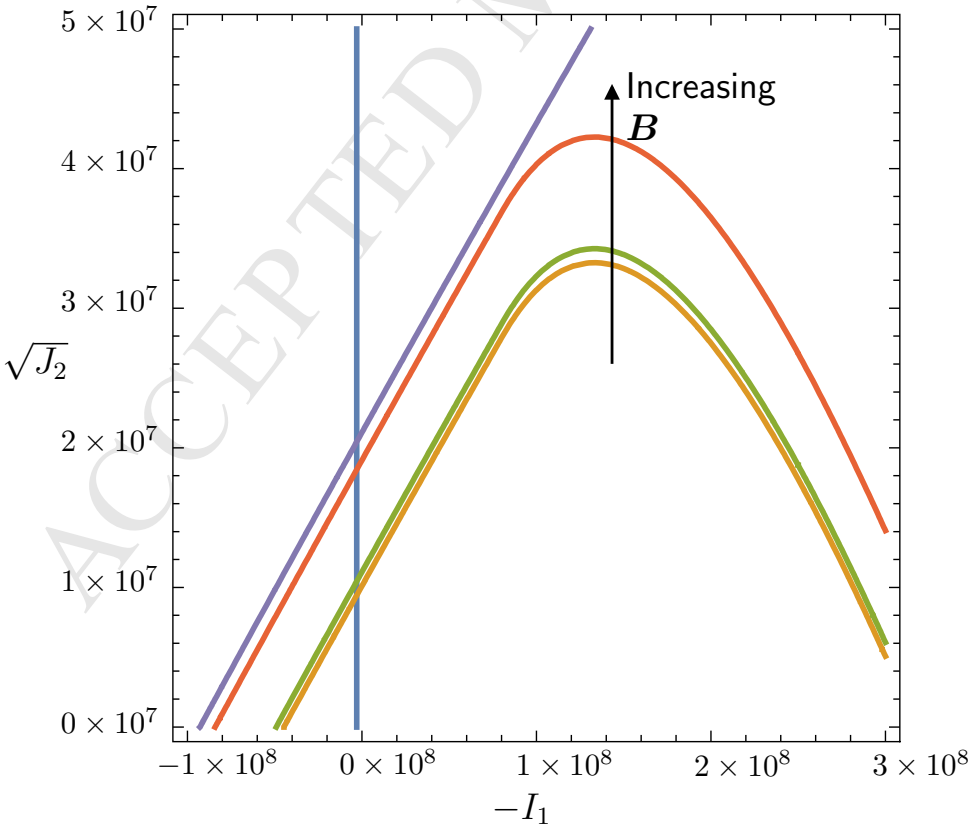

(b) Effect of kinematic hardening. $N = 12$ MPa.

Figure 4: Isotropic and kinematic hardening effects on the yield surface in the $-I_1, \sqrt{J_2}$ space.

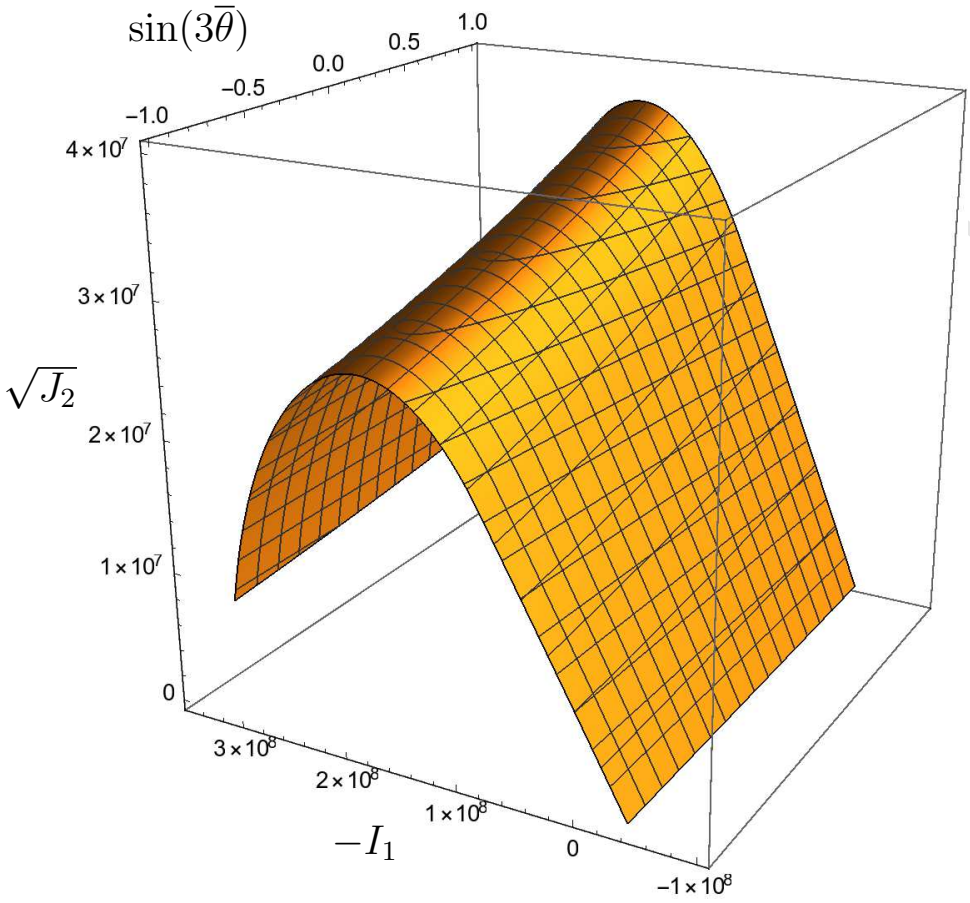

Figure 5: Limestone yield surface in $\sin\left(3\overline{\theta}\right), -I_1, \sqrt{J_2}$ space.

Table 2: Constitutive properties for basaltic magma

Mechanical properties obtained from [39], [13] and [35]			
Prop.	*Description*	*Value*	*Units*
κ	Bulk modulus	24.2×10^9	Pa
ν	Poisson coefficient	0.25	–
E	Elasticity modulus ($= 3\kappa(1-2\nu)$)	36.3×10^9	Pa
η	Viscosity [17]. $T \in [1448, 1623]$ K	$\exp\left(-38 + \frac{62\times10^3}{T}\right)$	Pa s
y	Initial yield stress (τ_1 in Chevrel *et al.* [13]) see also Piombo [29]	3.49×10^3	Pa

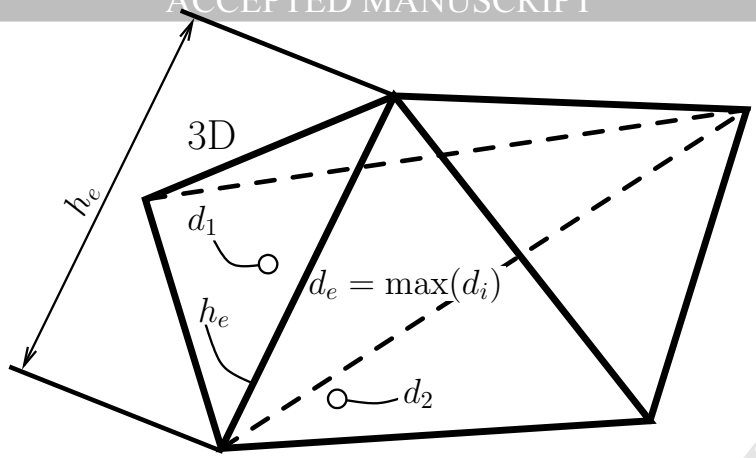

$$h_{opt} = (1 - d_e)h_e + d_e h_{\min}$$
$$h_{opt} < tol \cdot h_e \Rightarrow \text{mark edge for splitting}$$

Figure 6: Edge split condition based on edge length and the value of d.

5 Remeshing algorithm

Local remeshing is adopted to obtain sufficient resolution at the magma/limestone interface. This section presents the fundamental operations of the remeshing algorithm. We use the maximum of d_ε, d_s and d_p as an indicator for replacement of limestone by basaltic magma:

$$d = \max\left(d_\varepsilon, d_s, d_p\right) \tag{43}$$

Note that the rationale for this criterion is the loss of validity of the limestone yield surface when the failure surface is reached. A threshold value of d is used ($d_{\max} = 0.9$) such that replacement takes place when $d \geq d_{\max}$. Edge splitting takes place when the edge size condition is met:

$$\begin{aligned} &h_{\text{opt}} < tol \cdot h_e \\ &h_{\text{opt}} = (1 - d_e)h_e + d_e h_{\min} \end{aligned} \tag{44}$$

where $tol = 0.7$ and $h_{\min}$ is the minimum edge size which is here given as a problem data. d_e is the average d value of the surrounding elements of edge e.

In this process, three major steps are performed (1. edge marking, 2. creation of new nodes and elements, 3. mesh smoothing and mapping). Splitting edges is simpler than rotating edges (cf. [3]) since no specific crack path tracking is required. We classify each edge according to the maximum value of this mean d for adjacent elements, cf. 6. An optimal length h_{opt} is introduced and, if it is smaller than the actual edge length h_e, the edge is marked for splitting. A total of 11 independent subdivision cases are possible (removing cycles and symmetries) which are presented in Figure 7. Further details concerning this subdivision and the important aspect of avoiding Steiner-points is discussed in [4].

6 Verification test: compression of a cylindrical limestone block

A cylindrical specimen is used with $\oslash 50$ mm and $L = 100$ mm [23]. Figure 8 shows the dimensions and boundary conditions for this test. The first case consists of a monotonously increasing displacement $\overline{w}$ with confining pressure whereas the second case is a cyclic load. Contour plots for $\overline{\varepsilon}_v^p$, d_e, d_s and d_p are also shown. Two formulations (B-bar [37] and MINI [8]) are tested. Results are presented in Figures 9 for the reactions and 10 for d_e, d_p and d_s. for the two formulations and three values of confining pressure ($0, 10$ and 20 MPa). We conclude that the element formulation has a diminutive effect in the results and tetrahedra, which are more suitable to remeshing, can be used for limestone.

We note that ductility increases with increasing confining pressure and marked differences are observable between B-bar and the present assumed-strain formulation when low confining pressures are applied. For case II, we test the effect of kinematic hardening. In this case, there are differences between the two element formulations (see Figure 11), with slightly stiffer results for the B-bar formulation.

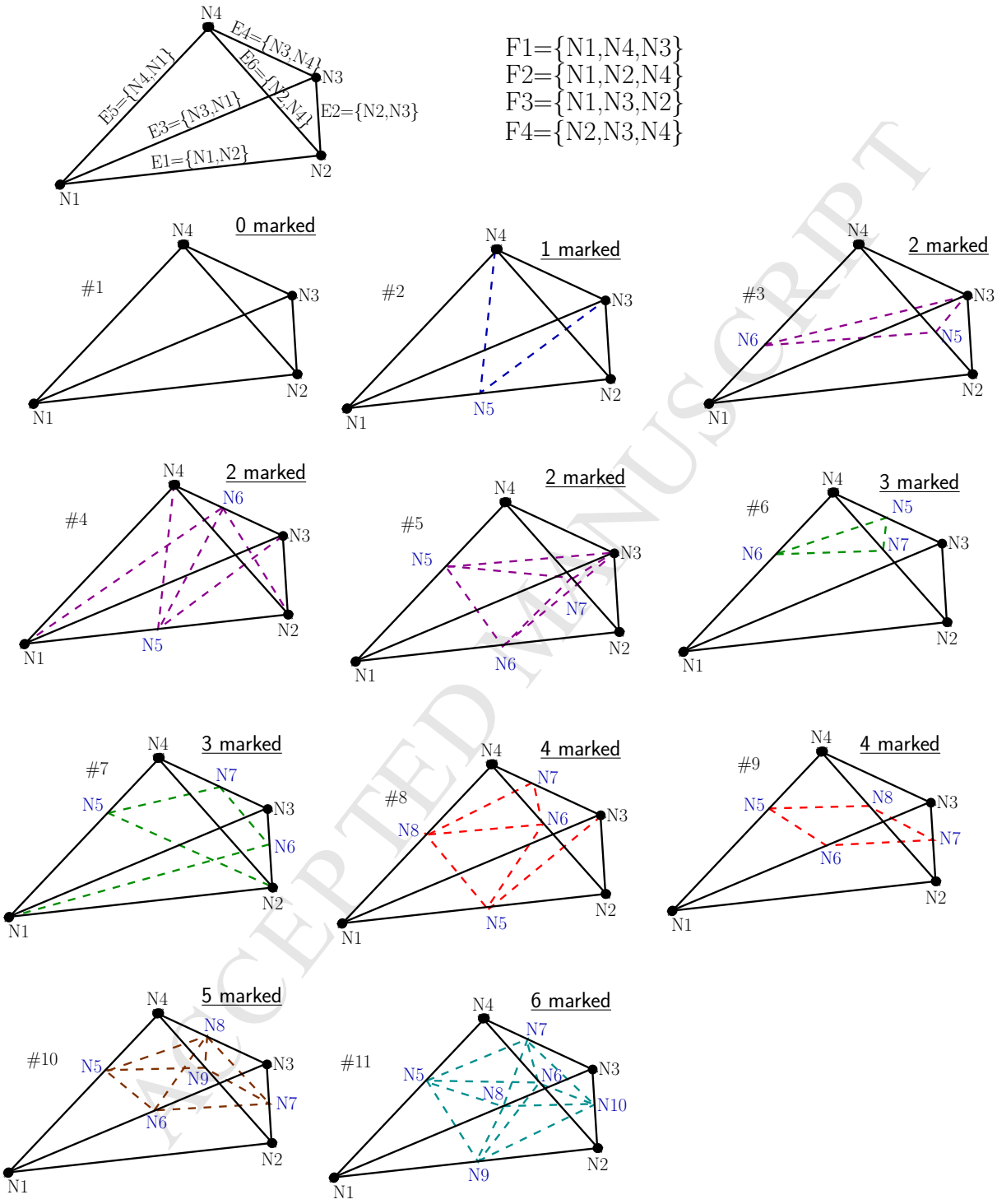

Figure 7: Tetrahedron subdivision: 11 independent cases (permutations and reflections removed). Node numbering for each case is in a one-to-one relation with local node numbering for each element. N_i are nodes ($i = 1, \ldots, 4, 5, \ldots, 10$), E_i are edges ($i = 1, \ldots, 6$) and F_i are faces ($i = 1, \ldots, 4$).

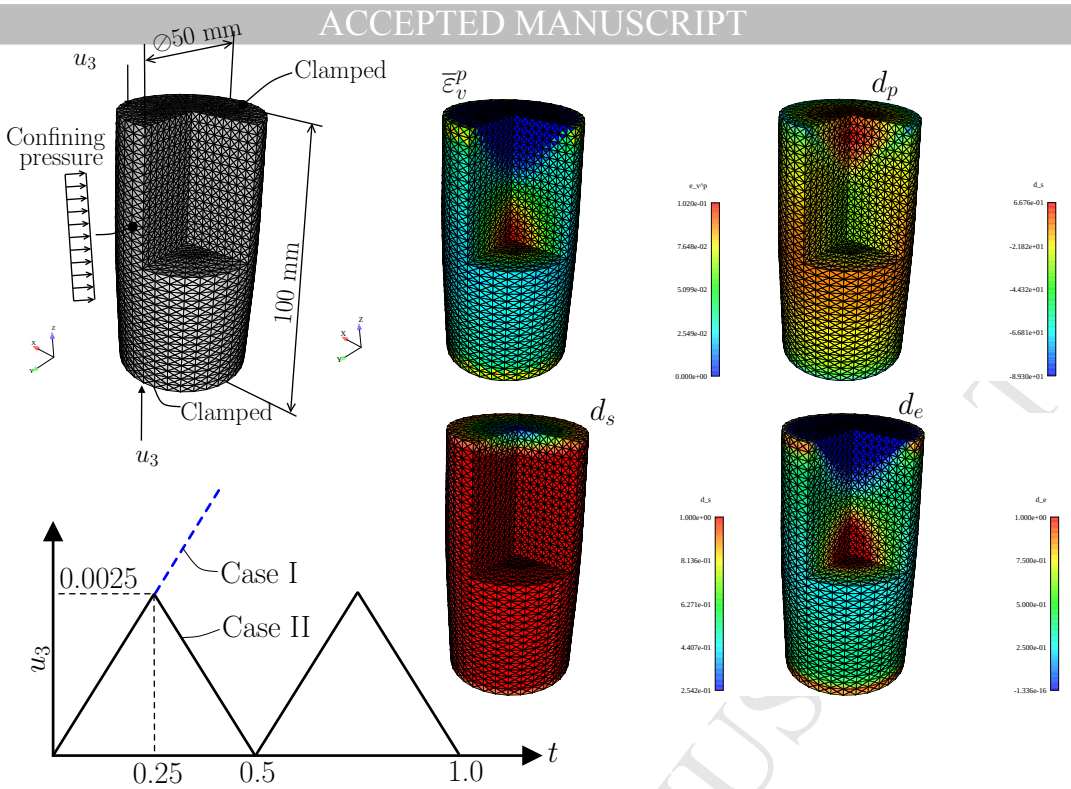

Figure 8: Limestone cylindrical specimen: dimensions and boundary conditions. The contour plots of $\overline{\varepsilon}_v^p$ and d_ε, d_s and d_p are also shown for $u_3 = 0.005$ m.

7 MINI Tetrahedron: element technology for quasi-incompressible problems

Elasto-plastic quasi-incompressible constitutive laws severely reduce the performance of displacement-based elements. Mixed elements are a solution for avoiding locking in quasi-incompressible problems. The low-order MINI element by Douglas Arnold ([8]), see also Bathe [10] and Cao [12], is based on a two-field formulation where:

- Pressure is linearly interpolated using the corner nodes.
- An internal shape function, named a bubble, enriches the displacement field.

Cauchy stress is calculated from the constitutive stress $\mathbf{S}_{ab}^{\star b}$ as:

$$\boldsymbol{\sigma}_a^a = \frac{1}{J_{ab}} \mathbf{S}_{ab} \tag{45}$$

The Cauchy pressure is obtained as:

$$p_a = -\frac{(\mathbf{S}_{ab})^T \mathbf{I}_3}{3 J_{ab}} \tag{46}$$

We can therefore write $\mathbf{S}_{ab}$ in Voigt form as a sum of deviatoric and pressure terms:

$$\mathbf{S}_{ab} = -J_{ab} p_a \mathbf{I}_3 + \mathbf{T}_{\text{dev}} \mathbf{S}_{ab} \tag{47}$$

where $\mathbf{T}_{\text{dev}}$ is the following sparse matrix:

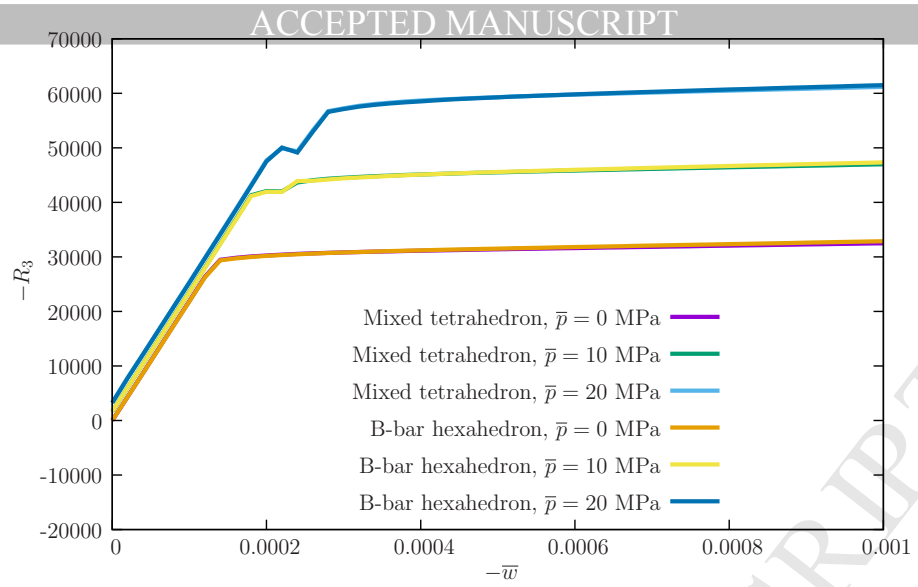

Figure 9: Limestone specimen: R_3-$\overline{w}$ results for case I.

$$\mathbf{T}_{\text{dev}} = \begin{bmatrix} \frac{2}{3} & -\frac{1}{3} & -\frac{1}{3} & 0 & 0 & 0 \\ -\frac{1}{3} & \frac{2}{3} & -\frac{1}{3} & 0 & 0 & 0 \\ -\frac{1}{3} & -\frac{1}{3} & \frac{2}{3} & 0 & 0 & 0 \\ 0 & 0 & 0 & 1 & 0 & 0 \\ 0 & 0 & 0 & 0 & 1 & 0 \\ 0 & 0 & 0 & 0 & 0 & 1 \end{bmatrix} \tag{48}$$

In terms of power balance, we use the following relation, where $\widetilde{\mathbf{S}}_{ab}$ depends on the independent pressure $\widetilde{p}$. It corresponds to a classical two-field variational principle:

$$\underbrace{\int_{\Omega_b} \left(\widetilde{\mathbf{S}}_{ab}\right)^T \dot{\mathbf{e}}^b_{ab} \mathrm{d}\Omega_b + \int_{\Omega_b} \left(J_{ab}\widetilde{p} + \frac{\left(\mathbf{S}_{ab}\right)^T \mathbf{I}_3}{3} \right) \dot{\widetilde{p}} \mathrm{d}\Omega_b}_{\dot{W}_{\text{int}}} = \dot{W}_{\text{ext}} \tag{49}$$

where the relative Jacobian J_{ab} is used to ensure correct volume calculation. We note that the product $J_{ab}\widetilde{p}$ cannot be used as an unknown field. In (49), we have the following quantities:

$$\widetilde{\mathbf{S}}_{ab} = -J_{ab}\widetilde{p}\mathbf{I}_3 + \mathbf{T}_{\text{dev}}\mathbf{S}_{ab} \tag{50}$$

Discretization follows the standard MINI formulation:

$$\boldsymbol{u}(\boldsymbol{\xi}) = \sum_{K=1}^{5} N_K(\boldsymbol{\xi})\, \boldsymbol{u}_K \tag{51}$$

Independent pressure $\widetilde{p}$ is interpolated using the corner nodes:

$$\widetilde{p}(\boldsymbol{\xi}) = \sum_{K=1}^{4} N_K(\boldsymbol{\xi})\, \widetilde{p}_K \tag{52}$$

Shape functions $N_K(\boldsymbol{\xi})$ are written according to their definition (cf. [18]):

$$N_1(\boldsymbol{\xi}) = 1 - \xi_1 - \xi_2 - \xi_3 \tag{53a}$$
$$N_2(\boldsymbol{\xi}) = \xi_2 \tag{53b}$$
$$N_3(\boldsymbol{\xi}) = \xi_3 \tag{53c}$$
$$N_4(\boldsymbol{\xi}) = \xi_1 \tag{53d}$$

The bubble function, for tetrahedra, is given by:

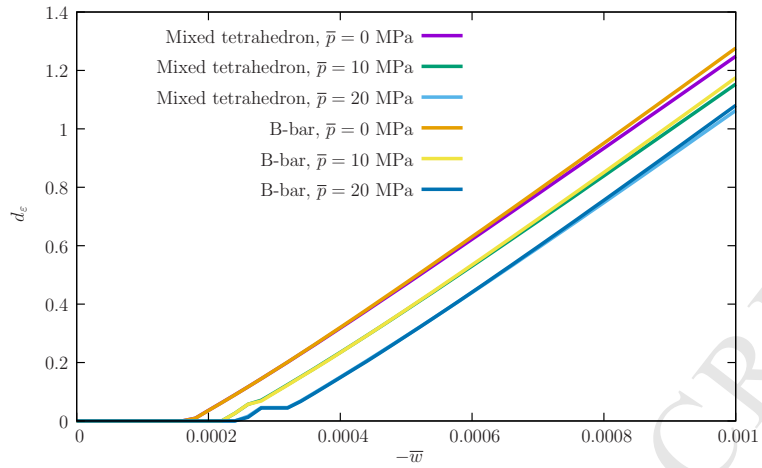

(a) $d_\varepsilon - \overline{w}$

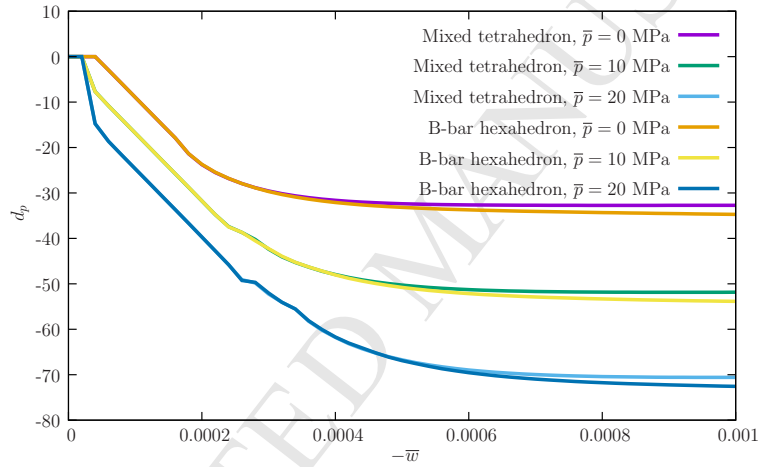

(b) $d_p - \overline{w}$

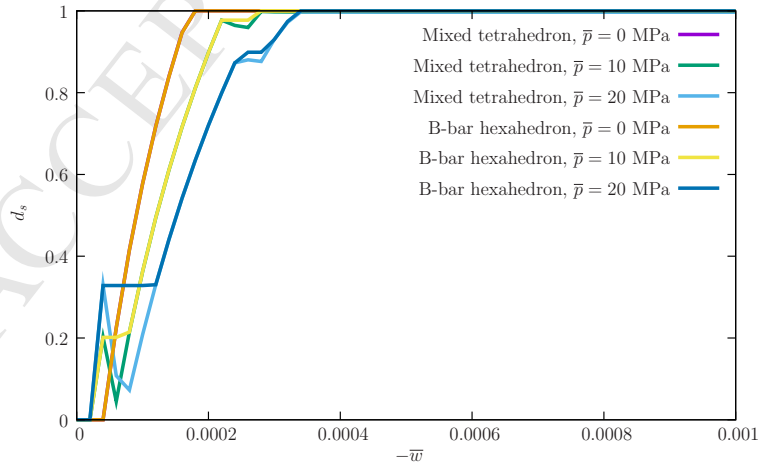

(c) $d_s - \overline{w}$

Figure 10: Limestone specimen: $d_\varepsilon - \overline{w}$, $d_p - \overline{w}$ and $d_s - \overline{w}$ for case I.

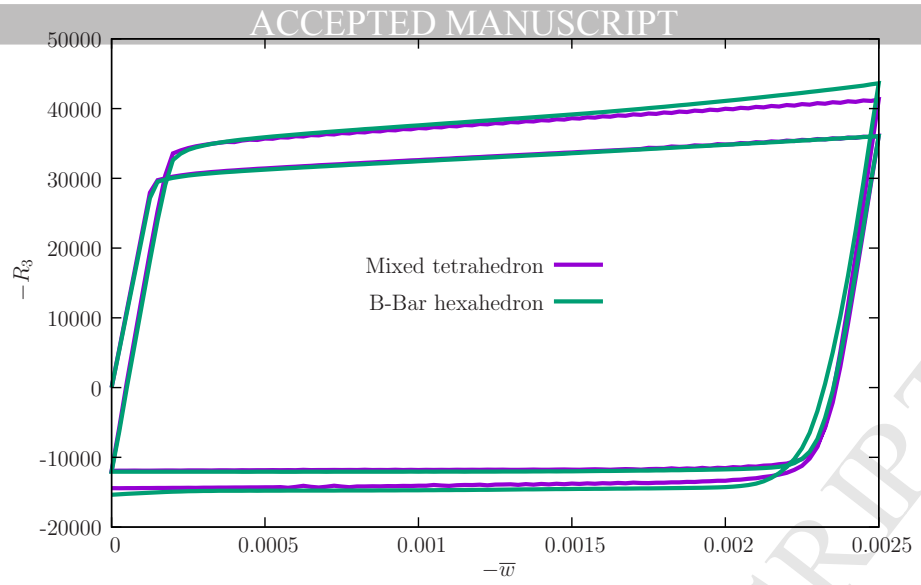

Figure 11: Limestone specimen: R_3-$\overline{w}$ results for case II cyclic loading results for $\overline{p} = 0$.

$$N_5(\boldsymbol{\xi}) = \xi_1\xi_2\xi_3\,(1 - \xi_1 - \xi_2 - \xi_3) \tag{53e}$$

For the calculation of the stiffness matrix, the variation of (49) is required. Not all quantities are determined by hand-derivation, and we use Mathematica [34] with the AceGen (cf. [21]) add-on to calculate some derivatives. Using (49), we obtain:

$$\begin{aligned} \mathrm{d}\dot{W}_{\mathrm{int}} &= \int_{\Omega_b} \left[\left(\mathrm{d}\widetilde{\mathbf{S}}_{ab}\right)^T \dot{\mathbf{e}}^b_{ab} + \left(\widetilde{\mathbf{S}}_{ab}\right)^T \mathrm{d}\dot{\mathbf{e}}^b_{ab} \right] \mathrm{d}\Omega_b && (54) \\ &\quad + \int_{\Omega_b} \left[\mathrm{d}J_{ab}\widetilde{p} + J_{ab}\mathrm{d}\widetilde{p} + \frac{(\mathrm{d}\mathbf{S}_{ab})^T \mathbf{I}_3}{3} \right] \dot{\widetilde{p}}\mathrm{d}\Omega_b && (55) \end{aligned}$$

where the following notation was used:

$$\begin{aligned} \mathrm{d}\mathbf{S}_{ab} &= \mathscr{C}_{ab}\mathrm{d}\mathbf{e}_{ab} && (56) \\ \mathrm{d}\widetilde{\mathbf{S}}_{ab} &= \mathbf{T}_{\mathrm{dev}}\mathscr{C}_{ab}\mathrm{d}\mathbf{e}^b_{ab} - \mathrm{d}J_{ab}\widetilde{p}\mathbf{I}_3 - J_{ab}\mathrm{d}\widetilde{p}\mathbf{I}_3 && (57) \end{aligned}$$

Specifically, the terms $\mathrm{d}\mathbf{e}_{ab}$ and $\mathrm{d}J_{ab}$ are determined by Mathematica with the AceGen add-on [34, 21].

8 Intrusion example

This section concerns the assessment of the proposed numerical technique by means of a benchmark application. SimPlas [1] (code 2281/D/17 ASSOFT), created by the first Author, was used. We now focus on an ellipsoid magma region within a block of limestone. Figure 13 shows the relevant data for this problem. For this example, the evolution of the mesh as a function of χV_i is provided in Figure 13 with detailed pictures. Growth starts near the outer edge of the ellipsoid and then bifurcation occurs and the magma flow reaches the outer faces of the limestone block. Damaged elements of limestone are progressively replaced by magma elements, whose volume growth is corrected to account for the difference. The evolution of the transversal displacement for seven distinct initial meshes is shown in Figure 14. This result shows that the appropriateness of our crack growth algorithm with replacement of materials. As mesh is refined, a shallower intrusion appears, but after some refinement, the magma region starts to converge to a stable thickness. Considering the complexity of this problem, reasonable agreement is observed. Mesh evolution for the seven distinct initial meshes is depicted in Figure 15.

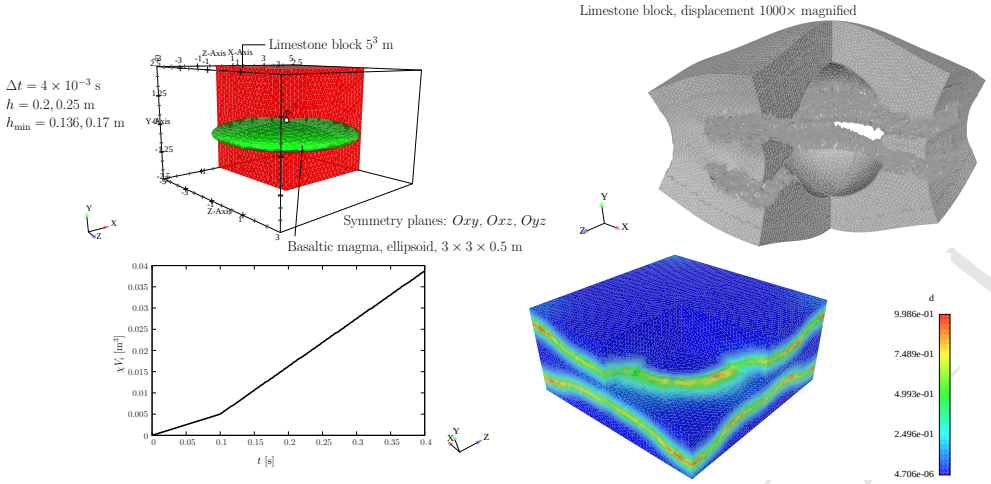

Figure 12: Intrusion example: geometry and relevant data. Magma was removed in the magnified depiction.

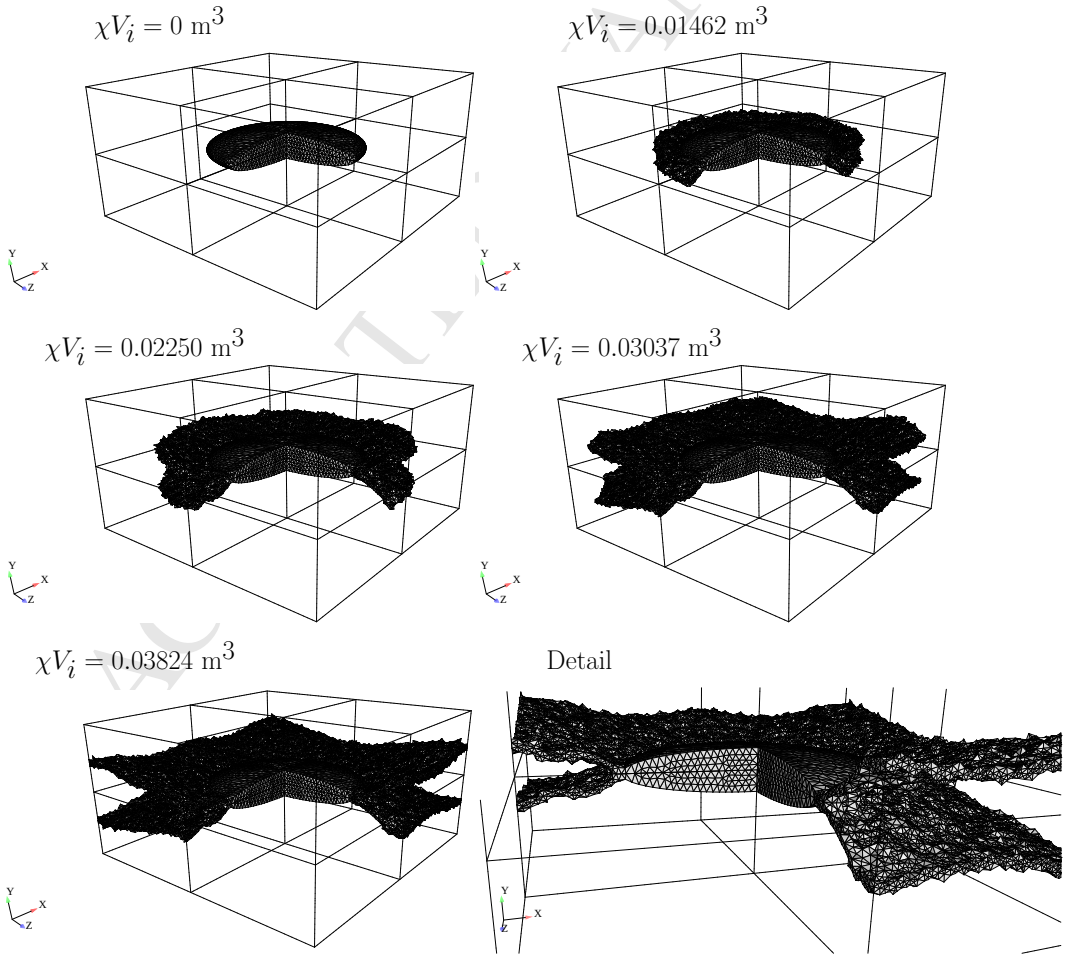

Figure 13: Magma intrusion in a limestone block.

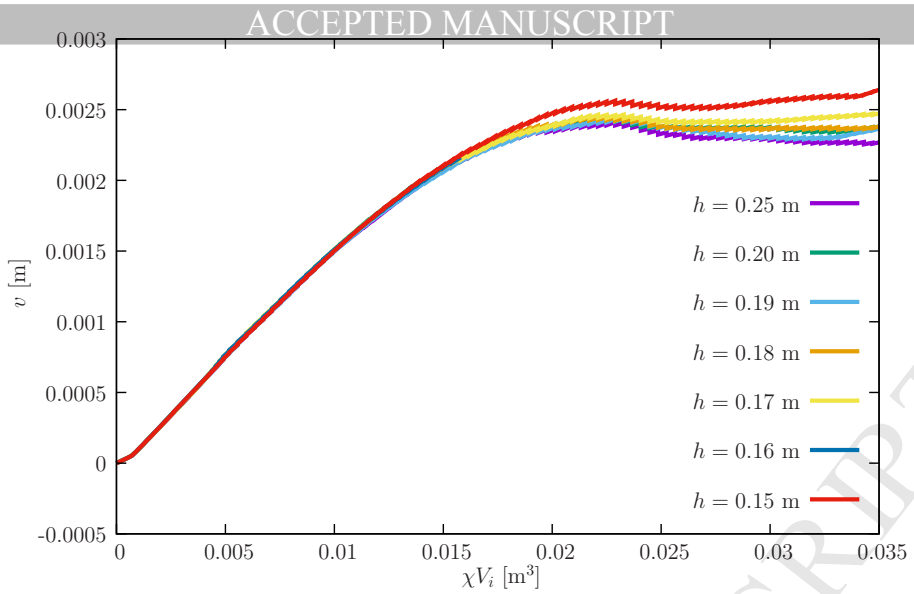

Figure 14: Mid-surface displacement evolution as a function of χV_i for seven initial mesh densities. Point P in Figure 12 is used.

9 Conclusions

Our framework was specialized to represent rock plasticity with kinematic hardening and rock fracture. It was able to simulate a magma basalt intrusion in a limestone block with a 3D tetrahedra model. Both basalt and limestone were represented with current constitutive laws and published properties. Crack in the basalt are filled with magma, whose volume growth is imposed. Mesh refinement was adopted to enhance the crack path resolution. Volume changes due to cracking are accounted for and therefore the initial mesh has only a moderate effect on the results. To correctly implement the mesh refinement algorithm, both stresses and back-stresses are stored in a global frame and transformed for constitutive integration. The MINI element was found to be sufficiently accurate for modeling finite strain plasticity and fracture. Intrusion results agree with the geological experience and the model will be further extended to account for thermo-mechanical coupling.

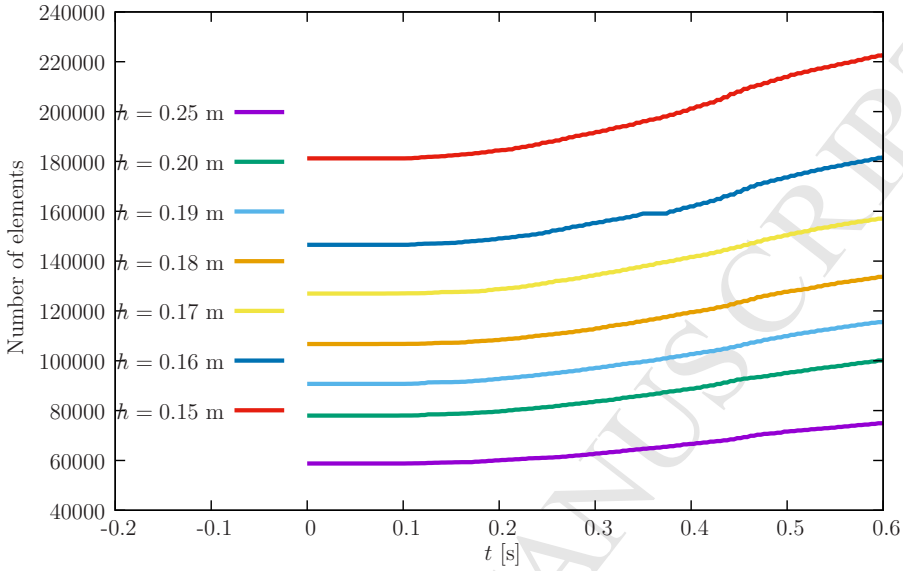

(a) Elements

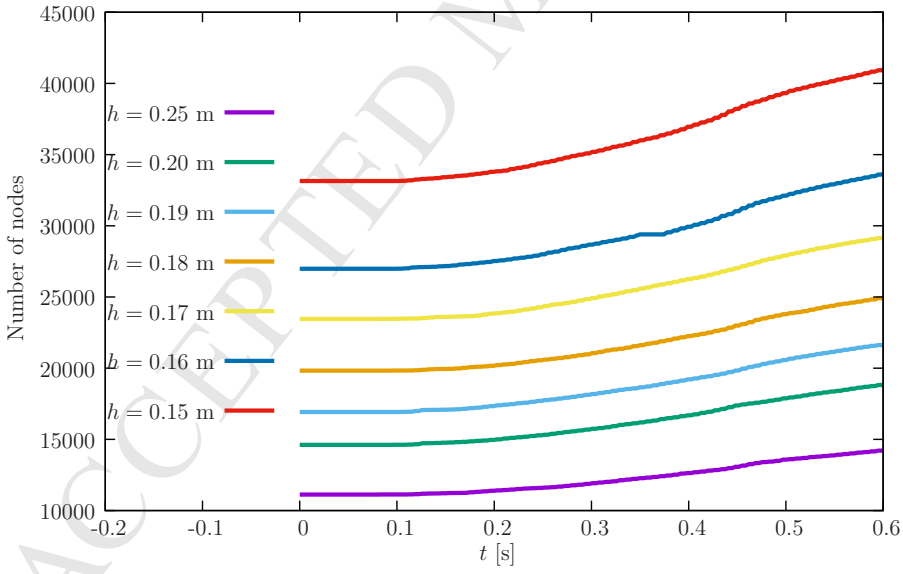

(b) Nodes

Figure 15: Mesh (nodes and elements) growth for the initial values of h. Seven initial meshes are tested ($h = 0.25$, 0.2, 0.19, 0.18, 0.17, 0.16 and 0.15 m).

References

[1] P. Areias. Simplas. http://www.simplas-software.com. Portuguese Software Association (ASSOFT) registry number 2281/D/17.

[2] P. Areias, R. Natal Jorge, J. César de Sá, T. Rabczuk, and J. Reinoso. General constitutive updating for finite strain formulations based on assumed strains and the jacobian. *Finite Elements in Analysis and Design*, 143:32–45, 2018.

[3] P. Areias and T. Rabczuk. Finite strain fracture of plates and shells with configurational forces and edge rotations. *Int J Numer Meth Eng*, 94:1099–1122, 2013.

[4] P. Areias and T. Rabczuk. Steiner-point free edge cutting of tetrahedral meshes with applications in fracture. *Finite Elem Anal Des*, 132:27–41, 2017.

[5] P. Areias, T. Rabczuk, J César de Sá, and J.L. Alves. Semi-implicit finite strain constitutive integration and mixed strain/stress control based on intermediate configurations. *Engineering Structures*, 124:344–360, 2016.

[6] P. Areias, J. Reinoso, P.P. Camanho, J. César de Sá, and T. Rabczuk. Effective 2d and 3d crack propagation with local mesh refinement and the screened poisson equation. *Engineering Fracture Mechanics*, 189:339–360, 2018.

[7] P.M.A. Areias and T. Belytschko. Analysis of three-dimensional crack initiation and propagation using the extended finite element method. *Int J Numer Meth Eng*, 63:760–788, 2005.

[8] D.N. Arnold, F. Brezzi, and M. Fortin. A stable finite element for the Stokes equations. *Calcolo*, XXI(IV):337–344, 1984.

[9] N.J. Balmforth, A.S. Burbidge, R.V. Craster, J. Salzig, and A. Shen. Visco-plastic models of isothermal lava domes. *Journal of Fluid Mechanics*, 403:37–65, 2000.

[10] K.-J. Bathe. *Finite Element Procedures*. Prentice-Hall, 1996.

[11] T. Belytschko, W.K. Liu, and B. Moran. *Nonlinear Finite Elements for Continua and Structures*. John Wiley & Sons, 2000.

[12] T.S. Cao, P. Montmitonnet, and P.O. Bouchard. A detailed description of the Gurson Tvergaard Needleman model within a mixed velocity pressure finite element formulation. *Int J Numer Meth Eng*, 96(9):561–583, 2013.

[13] M.O. Chevrel, T. Platz, E. Hauber, D. Baratoux, Y. Lavallée, and D.B. Dingwell. Lava flow rheology: A comparison of morphological and petrological methods. *Earth and Planetary Science Letters*, 384:109–120, 2013.

[14] J.D. Clemens and C.K. Mawer. Granitic magma transport by fracture propagation. *Tectonophysics*, 204:339–360, 1992.

[15] S. Dolarevic and A. Ibrahumbegovic. A modified three-surface elasto-plastic cap model and its numerical implementation. *Computers and Structures*, 85:419–430, 2007.

[16] A.F. Fossum and R.M. Brannon. The SANDIA geomodel: Theory and User's Guide. Technical Report SAND2004-3226 UC-405, Sandia National Laboratories, Albuquerque, New Mexico and Livermore, California, August 2004.

[17] M. Hobiger, I. Sonder, R. Büttner, and B. Zimanowski. Viscosity characteristics of selected volcanic rock melts. *Journal of Volcanology and Geothermal Research*, 200:27–34, 2011.

[18] T.J.R. Hughes. *The Finite Element Method*. Dover Publications, 2000. Reprint of Prentice-Hall edition, 1987.

[19] M.R. James, N. Bagdassarov, K. Mueller, and H. Pinkerton. Viscoelastic behaviour of basaltic lavas. *Journal of Volcanology and Geothermal Research*, 132:99–113, 2004.

[20] P. Kabele, J. Zak, and M. Somr. Finite-element modeling of magma chamber-host rock interactions prior to caldera collapse. *Geophysical Journal International*, 209:1851–1865, 2017.

[21] J. Korelc. Multi-language and multi-environment generation of nonlinear finite element codes. *Eng Computers*, 18(4):312–327, 2002.

[22] E. Lev, M. Spiegelman, and R.J. Wysocki. Investigating lava flow rheology using video analysis and numerical flow models. *Journal of Volcanology and Geothermal Research*, 247-248:62–73, 2012.

[23] D. Liu, C. Liu, Y. Kang, B. Guo, and Y. Jiang. Mechanical behavior of benxi formation limestone under triaxial compression: a new post-peak constitutive model and experimental validation. *Bulletin of Engineering Geology and the Environment*, November 2017. In Press.

[24] C. Miehe, F. Welschinger, and M. Hofacker. Thermodynamically consistent phase-field models of fracture: variational principles and multi-field fe implementations. *Int J Numer Meth Eng*, 83:1273–1311, 2010.

[25] R.W. Ogden. *Non-linear elastic deformations*. Dover Publications, Mineola, New York, 1997.

[26] J. Oliver. Continuum modelling of strong discontinuities in solid mechanics using damage models. *Comput Mech*, 17:49–61, 1995.

[27] M Paggi and J Reinoso. Revisiting the problem of a crack impinging on an interface: a modeling framework for the interaction between the phase field approach for brittle fracture and the interface cohesive zone model. *Computer Methods in Applied Mechanics and Engineering*, 2017.

[28] A. Philpotts and J. Ague. *Principles of Igneous and Metamorphic Petrology*. Cambridge University Press, Cambridge, United Kingdom, 2nd edition, 2009.

[29] A. Piombo and M. Dragoni. Evaluation of flow rate for a one-dimensional lava flow with power-law rheology. *Geophysical Research Letters*, 36(22), 2009. L22306.

[30] T. Rabczuk and T. Belytschko. Cracking particles: a simplified meshfree method for arbitrary evolving cracks. *Int J Numer Meth Eng*, 61(13):2316–2343, 2004.

[31] J Reinoso, M Paggi, and C Linder. Phase field modeling of brittle fracture for enhanced assumed strain shells at large deformations: formulation and finite element implementation. *Computational Mechanics*, pages 1–21, 2017.

[32] H. Ren, X. Zhuang, Y. Cai, and T. Rabczuk. Dual-horizon peridynamics. *Int J Numer Meth Eng*, 108(12):1451–1476, 2016.

[33] H. Ren, X. Zhuang, and T. Rabczuk. Dual-horizon peridynamics: A stable solution to varying horizons. *Comp Method Appl M*, 318:762–782, 2017.

[34] Wolfram Research Inc. Mathematica, 2007.

[35] E. Rivalta and P. Segall. Magma compressibility and the missing source for some dike intrusions. *Geophysical Research Letters*, 35(L04306):1–5, 2008.

[36] J.C. Simo and T.J.R. Hughes. *Computational Inelasticity*. Springer, corrected second printing edition, 2000.

[37] J.C. Simo, R.L. Taylor, and K.S. Pister. Variational and projection methods for the volume constraint in finite deformation elasto-plasticity. *Comp Method Appl M*, 51:177–208, 1985.

[38] I. Sonder, B. Zimanowski, and R. Buettner. Non-Newtonian viscosity of basaltic magma. *Geophysical Research Letters*, 33(L02303), 2006.

[39] F.J. Spera. Physical properties of magma. In H. Sigurdsson, B.F. Houghton, S.R. McNutt, H. Rymer, and J. Stix, editors, *Encyclopedia of Volcanoes*, pages 171–190. Academic Press, 1999.

[40] S.D.C. Walsh and M.O. Saar. Numerical models of stiffness and yield stress growth in crystal-melt suspensions. *Earth and Planetary Science Letters*, 267:32–44, 2008.

Highlights

August 30, 2018

- Coupled basaltic magma/limestone interaction with fracture.
- Dike intrusion by remeshing.
- Use of MINI element.
- Capped *Drucker-Prager* - *Bingham* fluid implementations in finite strains
- Smoothed complementarity implementation of plasticity.
- 3D Fracture verification test.